Fabricating highly active Pt atomically dispersed catalysts with the co-existence of Pt-O$_1$Ni$_1$ single atoms and Pt sub-nanoclusters for improved hydrogen evolution

Wei Xia [a], Mengyao Ma [a], Zhenhao Li [b], Liang Qiao [b], Kebin Chi [b], Xiaoyan Guo [a], Tianpeng Liu [a], Dengfeng Wu [a,*], Dong Cao [a,*], Daojian Cheng [a,*]

[a] State Key Laboratory of Organic-Inorganic Composites and College of Chemical Engineering, Beijing University of Chemical Technology, Beijing 100029, People's Republic of China
[b] PetroChina Petrochemical Research Institute, Beijing 102206, China

ARTICLE INFO

ABSTRACT

Atomically dispersed catalysts (ADCs), including single atoms and sub-nanoclusters, simultaneously, are considered as the most promising candidate to boost the reaction kinetics of hydrogen evolution reaction (HER). However, the correlation between the coordination environment of single atoms and catalytic activity has not been clearly discussed in ADCs system. Herein, Pt ADCs with the different coordination structures were fabricated by a facile sulfurate route coupling deposition strategy. Importantly, Pt ADCs, including Pt-O$_1$Ni$_1$ single atoms and Pt sub-nanoclusters (Pt$_{1+n}$/Ni$_3$S$_2$), show good basic HER activity, which just need 17 mV at 10 mA cm^{-2}. Meanwhile, the turnover frequency for Pt$_{1+n}$/Ni$_3$S$_2$ is 0.49 H$_2$ s^{-1} under the overpotential of 100 mV, which is 8.6 times higher than Pt/C. Besides, the assembled RuO$_2$ || Pt$_{1+n}$/Ni$_3$S$_2$ system could get 100 mA cm^{-2} current density under 1.7 V cell voltage in alkaline water electrolyzer. Notably, in-situ Raman and attenuated total reflection-surface enhanced infrared absorption spectroscopy reveal that Pt-O$_1$Ni$_1$ coordination is conducive to promoting the fracture of H-O-H bond, realizing the rapid transform of Pt-H* intermediates. Further, density functional theory calculations confirm Pt single atoms with Pt-O$_1$Ni$_1$ coordination environment in Pt$_{1+n}$/Ni$_3$S$_2$ serves as the main role for HER because Pt-O$_1$Ni$_1$ are more likely to accelerate the production of Pt-H* at the Pt sites, extremely achieving the rapid HER progress. This work discloses the structure-activity relationship in ADCs system, which is essential for the development of highly active electrocatalysts.

1. Introduction

Hydrogen is considered as a potential candidate for the future energy due to its high energy density and cleanliness [1–3]. Notably, the well-developed electrolytic water technology plays an important role to obtain green hydrogen [4–6]. Although Pt-based catalysts with unparalleled performance are still the most effective HER catalysts, the high cost of that is an important reason for limiting catalyst applications [7–11]. Meanwhile, the HER electrochemical kinetics is slower under alkaline conditions than that in acidic condition [12,13]. Therefore, it is particularly important to improve the hydrogen production activity of alkaline electrolytic water via developing the low-cost and high-active electrocatalysts.

In recent years, number of electrocatalysts, such as alloy materials

[14–17], multi-layered structure [18–20], and atomically dispersed catalysts (ADCs) with single atoms (SA) and nano-clusters (NC) [21–23], have been effectively reported for the water splitting in alkaline medium. It is worth noting that ADCs with the synergistic effect between SAs and NCs could extremely promote HER activity for alkaline. For example, Yang et al. [24] reported Ru ADCs loaded on N-doped porous carbon (Ru$_n$-Ru$_s$/NC), and Ru$_n$-Ru$_s$/NC have attached the current density of 10 mA cm^{-2} with only 37 mV in alkaline media. It should be attributed to the synergistic effect between Ru clusters and single atoms, which promoted Volmer dynamics to achieve excellent HER performance. Meanwhile, Pt ADCs, with Pt-O-Pt bridge on (Co, N) co-doped carbon substrate (Pt-AC/CoNC), have been reported to achieve excellent HER activity [25]. It was declared that Pt SAs would promote the adsorption of H* on Pt-O-Pt clusters and accelerate the desorption of H$_2$

molecules. Therefore, the ADCs simultaneously show great advantage in alkaline HER.

However, the single atoms in ADCs are extremely easy to aggregate on the surface of clusters to form particles, resulting in the deterioration of catalyst performance and stability in reaction [26,27]. The adjustment of coordination environment is an effective way that the aggregation would be gravely avoided as dispersed atoms via strong interactions with substrate and clusters, to achieve the high catalytic activity and stability [28–33]. For examples, Xu et al. [34] reported Ru ADCs (RuP/CoNi$_4$O$_{12}$) with adjustable coordination ligand atoms (O, P) numbers at the Ru sites. It was shown that the partial substitution of Ru-P bonds by Ru-O bonds can achieve rapid H$_2$O dissociation, thus exhibited excellent HER activity of 27 mV @10 mA cm^{-2} and 200 h @10 mA cm^{-2}. In addition, the length and number of coordination bonds could be used as the influence index for ADCs. The high temperature reduction strategy was used to realize the directional migration of Ti atoms to Pt atoms, shortening the length of Pt-Ti bonds to improve the oxidation activity and stability of CO [35]. However, the structure-activity relationship between single atoms ligand differences and properties is rarely reported. Therefore, it extremely prompts us to further research the coordination environment in ADCs system to improve the alkaline HER activity.

Here, to explore the relation between the activity and coordination structure of single atoms, we have successfully synthesized stable Pt ADCs with different coordination (Pt$_{1+n}$/Ni$_3$S$_2$ ADCs and Pt$_{1+n}$/NiS$_2$ ADCs). The coordination environment of Pt single atoms could be precisely regulated by changing the vulcanization method. More importantly, Pt$_{1+n}$/Ni$_3$S$_2$ with coordination structure of Pt-O$_1$Ni$_1$ requires only the overpotential of 17 and 73 mV to produce current density of 10 and 100 mA cm^{-2}, respectively. Besides, the good intrinsic activities for Pt$_{1+n}$/Ni$_3$S$_2$ of 479.7 mA mg$_{Pt}^{-1}$ and 0.49 H$_2$ s^{-1} are 8.7 and 8.6 times higher than Pt/C under the overpotential of 100 mV, respectively. Mechanism studies and in-situ characterizations reveal that Pt$_{1+n}$/Ni$_3$S$_2$ ADCs with Pt-O$_1$Ni$_1$ single atoms have excellent HER activity because Pt-O$_1$Ni$_1$ atoms are more likely to accelerate the transform of Pt-H* at the Pt sites. In addition, the presence of high-density nanosheets substrate also facilitates the full exposure of Pt single atom active sites to accelerate HER mass transfer process. The study provides a new horizon for the research of structure-activity relationship between atomic coordination and alkaline HER activity in atomically dispersed catalysts systems.

2. Synthesis experiment

2.1. Synthesis of Ni(OH)$_2$ nanosheets

0.34 mmol Ni (NO$_3$)$_2$·6 H$_2$O was dissolved with 12 mL methanol and 0.85 mL DMF. Then, the mixed solution was transferred to 25 mL of clean Teflon-lined autoclave with a clean Ni foam (2*2.5 cm^2) after ultrasonic homogenization. It was placed at 151.5 °C for 550 min. After the reaction was completed, the green material was clamped and rinsed with deionized water (DW) and ethanol. It was dried under vacuum at 40 °C for standby. The result catalyst is named as Ni(OH)$_2$. The XRD image was shown in Fig. S1 (Supporting Information).

2.2. Synthesis of Ni$_3$S$_2$ nanosheets

0.34 mmol Na$_2$S·9 H$_2$O was dissolved in 12 mL DW by using ultrasonic dispersion. Then, the solution was mixed with Ni(OH)$_2$ nanosheet in 25 mL Teflon-lined autoclave. After heating at 100 °C for 480 min, the catalyst was cooled to room temperature and washed with DW and ethanol. Then the back material was transferred to 40 °C vacuum to dry. The final catalyst is named Ni$_3$S$_2$.

2.3. Synthesis of NiS$_2$ nanosheets

First, Ni(OH)$_2$ was put into the magnetic boat in the air at a heating rate of 3 °/min to 300 °C for 120 min. After cooling to room temperature, the black NiO was took out. Then, 1 g S powder and NiO were placed in the upstream and downstream of quartz tube furnace, respectively. After introducing N$_2$, the temperature was heated to 300 °C with the heating rate of 3 °/min for 120 min. After cooling to room temperature, black NiS$_2$ catalyst was obtained.

2.4. Synthesis of Pt ADCs

0.12 mmol K$_2$PtCl$_4$ was dissolved in 1 M KOH solution (50 mL) to form electrodeposition solution. The stone grinding rod and mercury oxide electrode were used as the counter electrode and reference electrode, respectively. Then, Ni$_3$S$_2$ and NiS$_2$ were used as the working electrode to form three-electrode system, respectively. The reversible voltage was set to −0.506 V and kept 500 s. Finally, it was washed to remove the impurities on the surface with DW, and placed in 40 °C vacuum to dry. The synthetic sample is named Pt$_{1+n}$/Ni$_3$S$_2$ and Pt$_{1+n}$/NiS$_2$, respectively.

3. Result and discussion

3.1. Morphology Characterization

The electrodeposition strategy is one of the reliable methods for atomically dispersed catalysts [36,37]. As shown in Scheme 1, we successfully synthesized the Pt ADCs on nickel-based sulfides. To begin with, the scanning electron microscope (SEM) and transmission electron microscope (TEM) images were applied to reveal the presence of two-dimensional nanosheet structures of Ni$_3$S$_2$ and NiS$_2$ (Figs. S2 and S3, Supporting Information). Meanwhile, the lattice spacing of 0.235 and 0.200 nm should correspond to Ni$_3$S$_2$ (0 2 1) and NiS$_2$ (2 2 0) crystal planes detected by high-resolution TEM (HRTEM), respectively (Fig. S4). Besides, the corresponding energy dispersive X-ray (EDX) spectrums declare that Ni and S elements were uniformly distributed on Ni$_3$S$_2$ and NiS$_2$, respectively (Fig. S5). It is confirmed that the different nickel-based sulfides were successfully synthesized.

The morphology of Pt$_{1+n}$/Ni$_3$S$_2$ and Pt$_{1+n}$/NiS$_2$ were detected. As shown in Fig. S6, SEM and TEM images could further confirm the integrity of the two-dimensional nanosheet structure. The selected area electron diffraction (SAED) clearly confirms the existence of (0 2 1), (1 0 4), and (1 1 0) crystal planes of Ni$_3$S$_2$, respectively (Fig. 1a), it is consistent with the results of HRTEM (Fig. S7a). Then, the aberration-corrected high-angle annular dark-field scanning transmission electron microscopy (AC-HAADF-STEM) revealed the coexistence of Pt SAs and NCs nearby nickel atoms (Fig. 1b and c). Therefore, the ADCs system is confirmed for Pt$_{1+n}$/Ni$_3$S$_2$. In addition, the element mapping and element composition diagram of Pt$_{1+n}$/Ni$_3$S$_2$ reveal that Pt, Ni, O and S elements are uniformly distributed on the substrate (Fig. 1d and Fig. S7b). Similarly, two-dimensional nanosheet structure is detected for Pt$_{1+n}$/NiS$_2$ (Fig. S8), and NiS$_2$ (2 1 0) and (2 2 0) crystalline phase is detected for Pt$_{1+n}$/NiS$_2$ (Fig. 1e and Fig. S9a). Then, the Fig. 1f and g are also applied to reveal the existence of Pt ADCs for Pt$_{1+n}$/NiS$_2$. Besides, the element mapping and element composition diagram of Pt$_{1+n}$/NiS$_2$ further reveal that Pt, Ni and S elements are uniformly distributed on base (Fig. 1h and Fig. S9b). In summary, Pt$_{1+n}$/Ni$_3$S$_2$ and Pt$_{1+n}$/NiS$_2$ ADCs both were successfully certificated. The loading of Pt was determined to be 5.18 and 6.74 wt% by the inductively coupled plasma optical emission spectrometry (ICP-OES), respectively (Table S1).

3.2. Electronic interaction and coordination environment analysis

To explain the structure features of Pt$_{1+n}$/Ni$_3$S$_2$ and Pt$_{1+n}$/NiS$_2$ ADCs, X-ray diffraction (XRD), X-ray photoelectron spectroscopy (XPS)
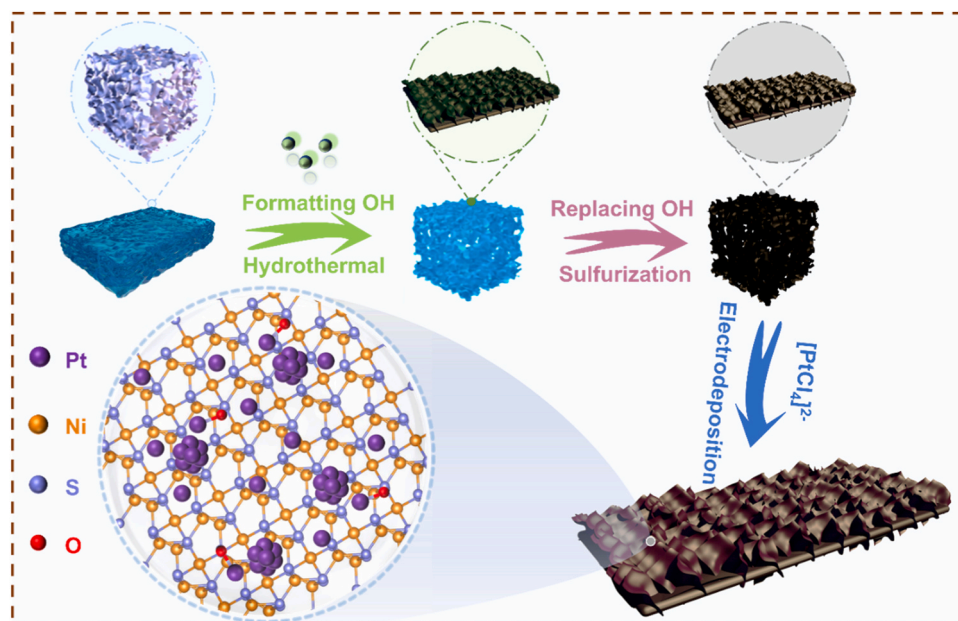
Scheme 1. The schematic diagram of Pt_{1+n}/Ni_3S_2 and Pt_{1+n}/NiS_2 electrocatalyst synthesis. The small ball in the figure represents different atoms, purple (Pt), orange (Ni), red (O), and blue (S).

and X-ray absorption spectroscopy (XAS) were applied. As shown as XRD analysis (Fig. 2a), those obvious characteristic peaks about Ni_3S_2 are detected. More importantly, no obvious peak about Pt nanoparticle is detected, further indicating the co-existence of Pt SAs and NCs. The lower diffraction peak intensity should be attributed to the partial reduction of the weaker metallic Ni-S bonds [38]. However, the existence of $Ni(OH)_2$ formed by the adsorption of OH^- on Ni surface effectively is conducive to the dispersion of Pt atoms [39–41]. Similarly, the crystal planes of NiS_2 are also obviously detected, and no Pt particle diffraction peaks. The above result is consistent with AC-HADDF-STEM analysis.

The XPS analysis was used to elucidate the surface valence state and electron interaction in different catalysts. The existence of Ni, S and O elements could be detected, and the signals of Pt atoms are detected only in Pt_{1+n}/Ni_3S_2 and Pt_{1+n}/NiS_2, confirming the successful introduction of Pt atoms (Fig. 2b). As shown in Fig. 2c, the orbits of Pt $4f_{7/2}$ and Pt $4f_{5/2}$ at 70.6 and 73.4 eV are attributed to Pt^0 [42,43]. For Pt_{1+n}/Ni_3S_2, the fitting peaks at 72.3 and 75.5 eV should be attributed to the higher oxidation state of Pt, which are higher than Pt_{1+n}/NiS_2 at 72.2 and 75.4 eV and Pt/C at 72.0 and 75.2 eV, respectively. Another peak near 67.9 eV is attributed to the Ni $3p$ of Ni^{2+} [44]. Meanwhile, Ni $2p_{5/2}$ and $2p_{3/2}$ fitting peaks of Ni^{2+} are located at 854.8 and 872.5 eV for Pt_{1+n}/Ni_3S_2 (Fig. 2d) [45–47]. Comparing with that of 854.5 and 872.2 eV for Ni_3S_2, the right shifts of 0.3 eV confirm electron transfer from Ni to Pt for Pt_{1+n}/Ni_3S_2. Similarly, the peaks of 854.7 and 872.6 eV confirm the presence of Ni^{2+} for Pt_{1+n}/NiS_2, and the fitting peaks of Ni $(OH)_2$ are also detected nearby 855.9 and 873.6 eV. As shown as Fig. 2e, the fitting peaks located at 162.4 and 163.6 eV in the S $2p_{3/2}$ and $2p_{1/2}$ fine spectrum are attributed to the Metal-S (M-S), and other is attributed to metal-sulphate bond [48]. The M-O bonds located at 530.4 and 530.6 eV of Pt_{1+n}/Ni_3S_2 and Pt_{1+n}/NiS_2 are moving forward with respect to Ni_3S_2 and NiS_2 in Fig. 2f, and the $Ni(OH)_2$ fitting peaks was located at other peak [49].

XAS analysis, including X-ray absorption near-edge structure (XANES) spectrum and extended X-ray absorption fine structure (EXAFS), was applied to investigate the coordination environment of Pt atoms for different electrocatalyst. The normalized absorption spectrogram was corrected by the reference spectrogram (Fig. 3a and Fig. S10). Generally, the position of the white-line peak formed by the orbital

transition from Pt $2p$ to Pt $5d$ orbital is closely related to the oxidation state of the central part [37]. As shown in Fig. S11, the average valence states of Pt atoms are +1.1 and +0.6 for Pt_{1+n}/Ni_3S_2 and Pt_{1+n}/NiS_2, respectively. Further, the Pt L-edge FT-EXAFS spectrums of different samples were plotted via the k-space oscillating waveform function curves (Fig. 3b and Fig. S12a). The FT-EXAFS curves of Pt_{1+n}/Ni_3S_2 show obvious coordination peak at 1.75 Å, which should be attributed to Pt-O bonds derived from OH^- on Pt surface (Pt-OH). However, the bonds at 1.98 Å for Pt_{1+n}/NiS_2 are attributed to the influence of Pt-S [50], showing that Pt atoms are mainly deposited on the surface of S. Therefore, the adjustment of the coordination environment is regarded as an important reason for the different performance between Pt_{1+n}/Ni_3S_2 and Pt_{1+n}/NiS_2. Afterwards, the quantitative EXAFS fitting analyses were performed to determine the specific coordination numbers of Pt atoms for different catalysts (Fig. 3c and d). It is confirmed that Pt_{1+n}/Ni_3S_2 has satisfied Pt-O first shell coordination and Pt-Ni second shell coordination, and the coordination numbers of Pt-O and Pt-Ni both are 1 with the bonding distances of 1.97 Å and 2.54 Å, respectively [51]. Similarly, for Pt_{1+n}/NiS_2, the coordination numbers of Pt-S and Pt-Ni are 2 (2.60 Å) and 2 (2.65 Å), respectively (Table S2). In addition, the study has shown that lower coordination number could promote the adsorption of H* at Pt sites, thus achieving excellent HER kinetics [52]. Therefore, Pt_{1+n}/Ni_3S_2 with $Pt-O_1Ni_1$ coordination achieves excellent HER kinetics in alkaline media. Besides, the wavelet transform (WT) spectrum of Pt_{1+n}/Ni_3S_2 catalysts exhibit the largest coordination strengths of Pt-O bond at R≈1.6 Å/k≈10.7 $Å^{-1}$, but Pt_{1+n}/NiS_2 catalysts display the strengths of Pt-S bond at R≈1.8 Å/k≈7.5 $Å^{-1}$, respectively (Fig. 3e). Similarly, the oxidation state of Ni for Pt_{1+n}/Ni_3S_2 and Pt_{1+n}/NiS_2 both are very close to Ni^{2+} (Fig. 3f), which indicates that Ni atoms exhibit certain oxidation state characteristics. It is consistent with the results presented by XPS. The K-edge FT curves of different samples were obtained, and it was confirmed that Pt_{1+n}/Ni_3S_2 and Pt_{1+n}/NiS_2 showed similar Ni-O, Ni-Ni and Ni-S-Ni coordination peaks at 1.60, 2.75, and 3.61 Å, respectively (Fig. 3g) [53]. The Ni-Pt-(Ni) bonds of Pt_{1+n}/Ni_3S_2 (2.70 Å) and Pt_{1+n}/NiS_2 (2.72 and 3.97 Å) were fitted, respectively (Table S3). At the same time, wavelet transform spectra images of different catalysts were obtained by k^3-weighted spectra (Fig. 3h, Fig. S12b and Fig. S13), which was consistent with the Pt L-edge FT-EXAFS results. Finally, the q-space
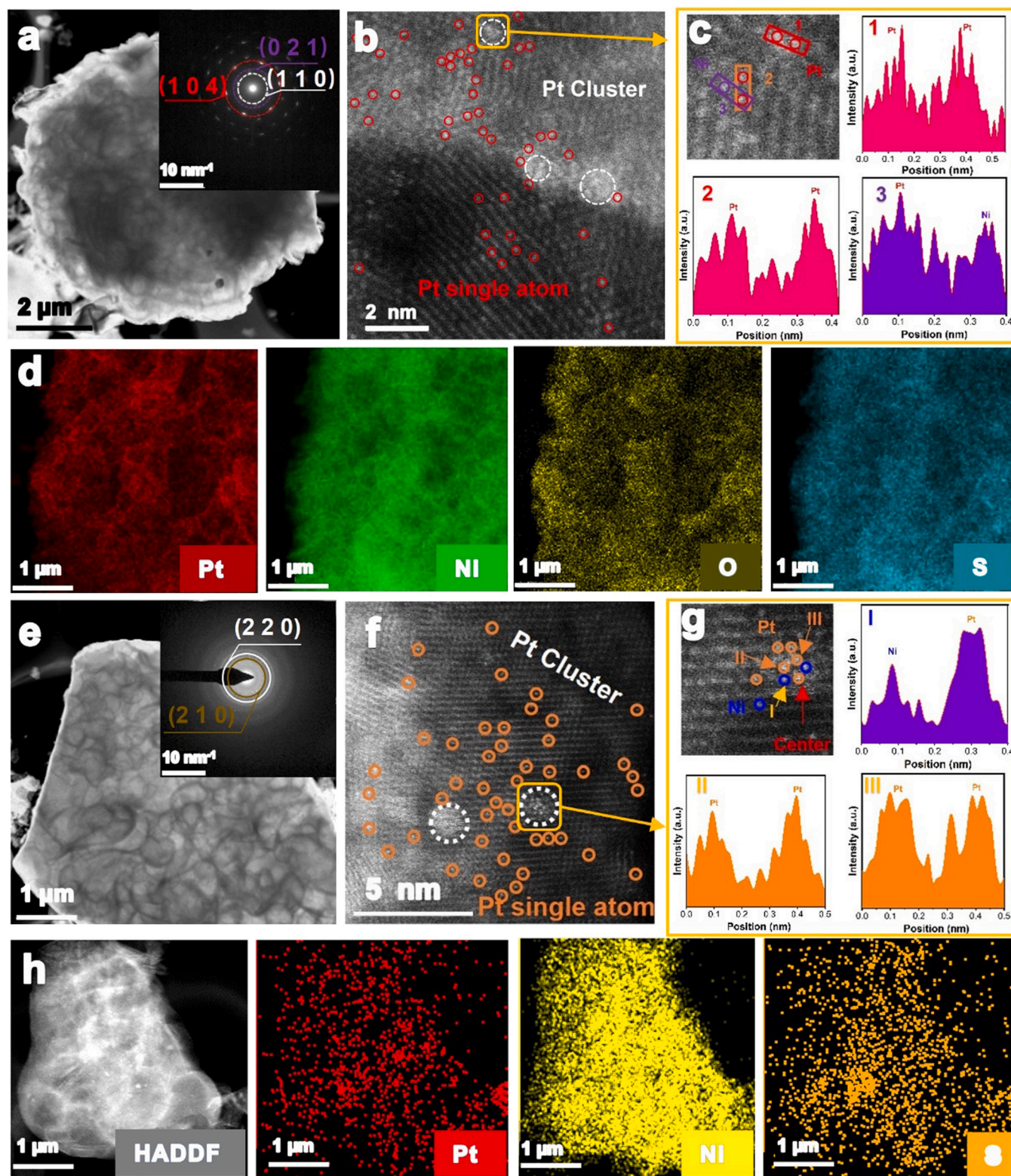
Fig. 1. (a) The STEM pattern of Pt_{1+n}/Ni_3S_2. The insert showed the selected area electron diffraction (SAED) pattern of Pt_{1+n}/Ni_3S_2 ADCs. (b) The AC-STEM pattern of Pt_{1+n}/Ni_3S_2. Pt single atoms (red) and Pt clusters (white). (c) AC-STEM images and the corresponding extracted line profiles of Pt_{1+n}/Ni_3S_2. (d) The corresponding elemental mapping pattern about Pt, Ni, O and S of Pt_{1+n}/Ni_3S_2, respectively. (e) The STEM pattern of Pt_{1+n}/NiS_2 ADCs. The insert showed the SAED pattern of Pt_{1+n}/NiS_2. (f) The AC-STEM pattern of Pt_{1+n}/NiS_2 catalyst. Pt single atoms (orange) and Pt clusters (white). (g) AC-STEM images and the corresponding extracted line profiles of Pt_{1+n}/NiS_2. (h) The corresponding HADDF and elemental mapping pattern about Ni, Pt and S of Pt_{1+n}/NiS_2, respectively.

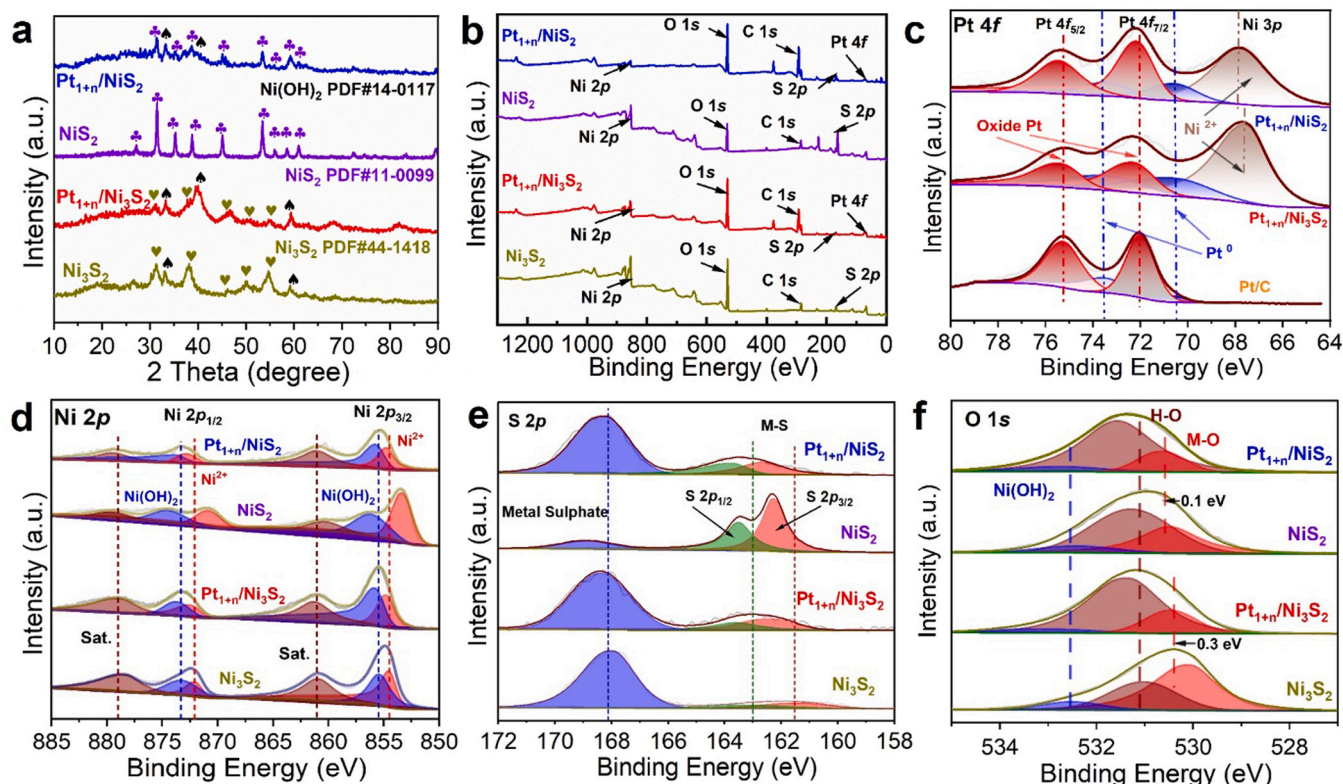**Fig. 2.** (a) The XRD pattern for Pt_{1+n}/Ni_3S_2, Pt_{1+n}/NiS_2, Ni_3S_2, and NiS_2 catalyst, respectively. (b) The spectrum of X-ray photoelectron spectroscopy for Pt_{1+n}/Ni_3S_2, Pt_{1+n}/NiS_2, Ni_3S_2, and NiS_2 catalyst, respectively. The fine spectrogram of (c) Pt $4f$ orbit, (d) Ni $2p$ orbit, (e) S $2p$ orbit, and (f) O 1 s orbit for different catalyst, respectively.

EXAFS fitting curve of Pt_{1+n}/Ni_3S_2 and Pt_{1+n}/NiS_2 about Pt L-edge and Ni K-edge was shown in Fig. S14, to confirm that the fitting curve coincided with the test data. Therefore, the difference of coordination environment is as the direct evidence that the difference of HER catalytic activity.

3.3. The performance of HER

To truly reflect the polarization ability of the catalysts, the HER performance, including that of Pt_{1+n}/Ni_3S_2, Pt_{1+n}/NiS_2, Ni_3S_2, NiS_2 and Pt/C catalysts, were tested under the scanning rate of 1 mV s^{-1} in three electrode system in 1 M KOH [54]. The reference was corrected before using and the LSV curves of all catalysts were obtained via 85% potential compensation. As showed as Fig. 4a and b, it is worth noting that Pt_{1+n}/Ni_3S_2 catalyst only needed the overpotential of 17 mV to drive current density of 10 mA cm^{-2} in 1 M KOH electrolyte, which is lower than that of commercial Pt/C (48 mV) and Pt_{1+n}/NiS_2 (49 mV), respectively. It should be attributed to the $Pt-O_1Ni_1$ coordination structure formed by the electronegative O atoms, resulting in Pt_{1+n}/Ni_3S_2 have relatively good HER catalytic activity. Besides, Pt_{1+n}/Ni_3S_2 (73 mV) shows good HER catalytic activity than Pt_{1+n}/NiS_2 (140 mV) and Pt/C (185 mV) surpass large current density of 100 mA cm^{-2}. The tafel fitting curves were revealed in Fig. 4c. The Tafel fitting value of Pt_{1+n}/Ni_3S_2 displays as 14.6 mV dec^{-1}, which is lower than Pt/C (28.3 mV dec^{-1}), Pt_{1+n}/NiS_2 (33.2 mV dec^{-1}), Ni_3S_2 (75.5 mV dec^{-1}) and NiS_2 (125.7 mV dec^{-1}), respectively. Meanwhile, the fact is confirmed that highly electronegative oxygen in Pt-O bond provides H* receptor, which accelerates the adsorption of H* and the conversion of intermediate Pt-H* [55]. Therefore, Pt_{1+n}/Ni_3S_2 has better reaction kinetics than Pt_{1+n}/NiS_2.

The exchange current density obtained from the Tafel fitting curves could explain the internal driving force of HER reaction (Fig. S15a). It can be found that Pt_{1+n}/Ni_3S_2 (0.94 mA cm^{-2}) is superior to Pt_{1+n}/NiS_2

(0.50 mA cm^{-2}), Pt/C (0.30 mA cm^{-2}), Ni_3S_2 (0.13 mA cm^{-2}) and NiS_2 (0.20 mA cm^{-2}), respectively, which confirms Pt_{1+n}/Ni_3S_2 exhibits better polarization ability than above catalysts. Electrochemical impedance spectroscopy (EIS) is often used to evaluate electron transfer capacity. As shown as Fig. S15b, it is impressive that Pt_{1+n}/Ni_3S_2 has smaller charge transfer resistance (R_{ct}) of 1.3 Ω under 10 mA cm^{-2} current density than Pt/C (1.4 Ω), Pt_{1+n}/NiS_2 (1.6 Ω) and the precursors (2.8 Ω). It indicates the rapid transfer ability of Pt_{1+n}/Ni_3S_2. The electrochemical active surface areas (ECSAs) is used as an important parameter to prove intrinsic activity, which is in direct proportion to the double layer capacitance (C_{dl}) [56]. The CV curves with different samples were displayed in Figs. S16 and S17. As shown in Fig. 4d, it is obvious that Pt_{1+n}/Ni_3S_2 shows the largest C_{dl} value of 50.66 mF cm^{-2} among samples, which is close to Pt/C (49.46 mF cm^{-2}), but much higher than Pt_{1+n}/NiS_2 (25.78 mF cm^{-2}), Ni_3S_2 (11.33 mF cm^{-2}) and NiS_2 (14.91 mF cm^{-2}), respectively. Moreover, the current density of Pt_{1+n}/Ni_3S_2 normalized by the ECSAs is maximum at the same overpotential than mentioned catalysts (Fig. S18a), confirming that Pt_{1+n}/Ni_3S_2 have better intrinsic catalytic activity.

The mass activity curves of different Pt catalysts were shown in Fig. S18b, and the mass and molar mass loading of Pt with different catalysts were recorded to Table S4 (375 μg/cm^2 for Pt_{1+n}/Ni_3S_2). From the left side of Fig. 4e, it could be seen that Pt_{1+n}/Ni_3S_2 and Pt_{1+n}/NiS_2 display the better mass active of 479.7 and 347.0 mA mg$_{Pt}^{-1}$ under the overpotential of 100 mV, respectively. More importantly, the mass active of Pt_{1+n}/Ni_3S_2 is 8.7 times higher than Pt/C (57.1 mA mg$_{Pt}^{-1}$). Similarly, the turnover frequency (TOF) of Pt_{1+n}/Ni_3S_2 and Pt_{1+n}/NiS_2 are 0.49 and 0.35 H$_2$ s^{-1} at the overpotential of 100 mV, respectively (the right side of Fig. 4e and Fig. S18c), and that of Pt_{1+n}/Ni_3S_2 is 8.6 times higher than Pt/C. Therefore, the preferable intrinsic activity of Pt_{1+n}/Ni_3S_2 is indicated. Finally, Pt_{1+n}/Ni_3S_2 exhibits more 110 h stability under 200 mA cm^{-2} current density, and the performance is not significantly reduced after the CV test of 3000 circles (Fig. 4f). It is
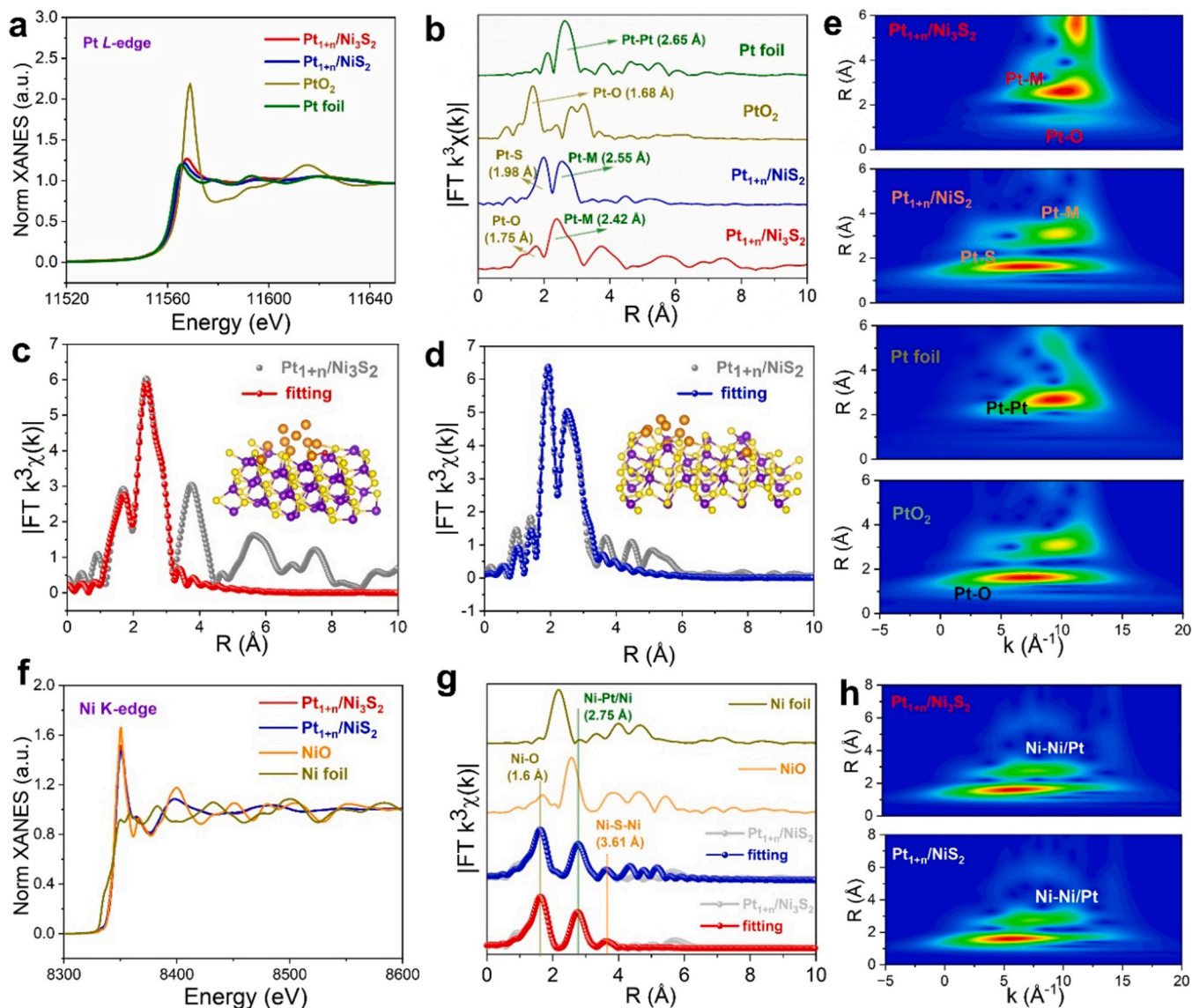
Fig. 3. (a) The normalized XANES spectra at the Pt L-edge about Pt_{1+n}/Ni_3S_2, Pt_{1+n}/NiS_2, Pt foil, and PtO_2, respectively. (b) The k^3-weighted FT-EXAFS spectra for Pt_{1+n}/Ni_3S_2, Pt_{1+n}/NiS_2, Pt foil, and PtO_2, respectively. (c) The EXAFS fitting curves of Pt_{1+n}/Ni_3S_2 at the R space. The inset corresponds to the atomic structures. (d) The EXAFS fitting curves of Pt_{1+n}/NiS_2 at the R space. The inset corresponds to the atomic structures. (e) The wavelet transforms image (WT) for the k^3-weighted EXAFS spectra of Pt_{1+n}/Ni_3S_2, Pt_{1+n}/NiS_2, Pt foil, and PtO_2, respectively. M was regarded as Pt and Ni. (f) The normalized XANES spectra at the Ni K-edge about Pt_{1+n}/Ni_3S_2, Pt_{1+n}/NiS_2, Ni foil, and NiO, respectively. (g) The k^3-weighted FT-EXAFS spectra for Pt_{1+n}/Ni_3S_2, Pt_{1+n}/NiS_2, Ni foil, and NiO, respectively. The fitting curves of Pt_{1+n}/Ni_3S_2 and Pt_{1+n}/NiS_2, respectively. (h) The WT image for the Ni-K k^3-weighted EXAFS spectra of Pt_{1+n}/Ni_3S_2 and Pt_{1+n}/NiS_2, respectively.

indicated that Pt_{1+n}/Ni_3S_2 has excellent stability. Notably, Pt_{1+n}/Ni_3S_2 also exhibits decent performance than the current outstanding atomically dispersed HER catalysts (Fig. 4g and Table S5). The stability of Pt_{1+n}/NiS_2 was showed in Fig. S18d. To summary up, the reported Pt_{1+n}/Ni_3S_2 exhibits good HER catalytic activity, which proves that Pt ADCs with single atoms binding highly electronegative ligand is more conducive to promoting HER dynamics and stability. To discuss the potential capacity of Pt_{1+n}/Ni_3S_2 for industrial applications, RuO_2 || Pt_{1+n}/Ni_3S_2 was assembled at the flowing alkaline water electrolyzer (AWE). It is worth noting that the RuO_2 || Pt_{1+n}/Ni_3S_2 system could achieve high current density of 100 and 500 mA cm^{-2} under 1.7 and 2.0 V under 353 K conditions, respectively (Fig. 5a). The inset is a schematic of AWE. In addition, the mass active of RuO_2 || Pt_{1+n}/Ni_3S_2 system (1.35 A mg$_{Pt}^{-1}$) is 3.75 folds higher than that of RuO_2 || Pt/C system (0.36 A mg$_{Pt}^{-1}$) under 2.0 V cell voltage (Fig. S19), showing decent mass intrinsic activity in AWE system. Besides, Fig. 5b exhibits excellent stability at large current density of 100 mA cm^{-2}, indicates

that Pt_{1+n}/Ni_3S_2 ADCs could be used as potential candidates for the development of efficient alkaline water electrolytic catalysts.

3.4. Structure and component stability

To further determine the stability of the composition and structure after stability tests in 1 M KOH solution, the XRD, TEM and XPS measurements for Pt_{1+n}/Ni_3S_2 and Pt_{1+n}/NiS_2 after stability tests were carried. It is worth noted that the morphology of Pt_{1+n}/Ni_3S_2 and Pt_{1+n}/NiS_2 still show the nanosheet structure after stability tests (Figs. S20 and S21). Besides, the XRD pattern was determined after stability tests for Pt_{1+n}/Ni_3S_2 and Pt_{1+n}/NiS_2 (Fig. 5c). The lattice spacing of 0.235 nm belongs to the Ni_3S_2 (0 2 1) phase for Pt_{1+n}/Ni_3S_2 (Fig. 5d), which is the same as the initial phase. It is consistent with SAED results (the upper left of the insert). Then, the AC-HAADF-STEM images for Pt_{1+n}/Ni_3S_2 after stability test revealed the coexistence of Pt SAs and NCs on nickel sulfide (Fig. 5e), confirming Pt_{1+n}/Ni_3S_2 after stability tests still present

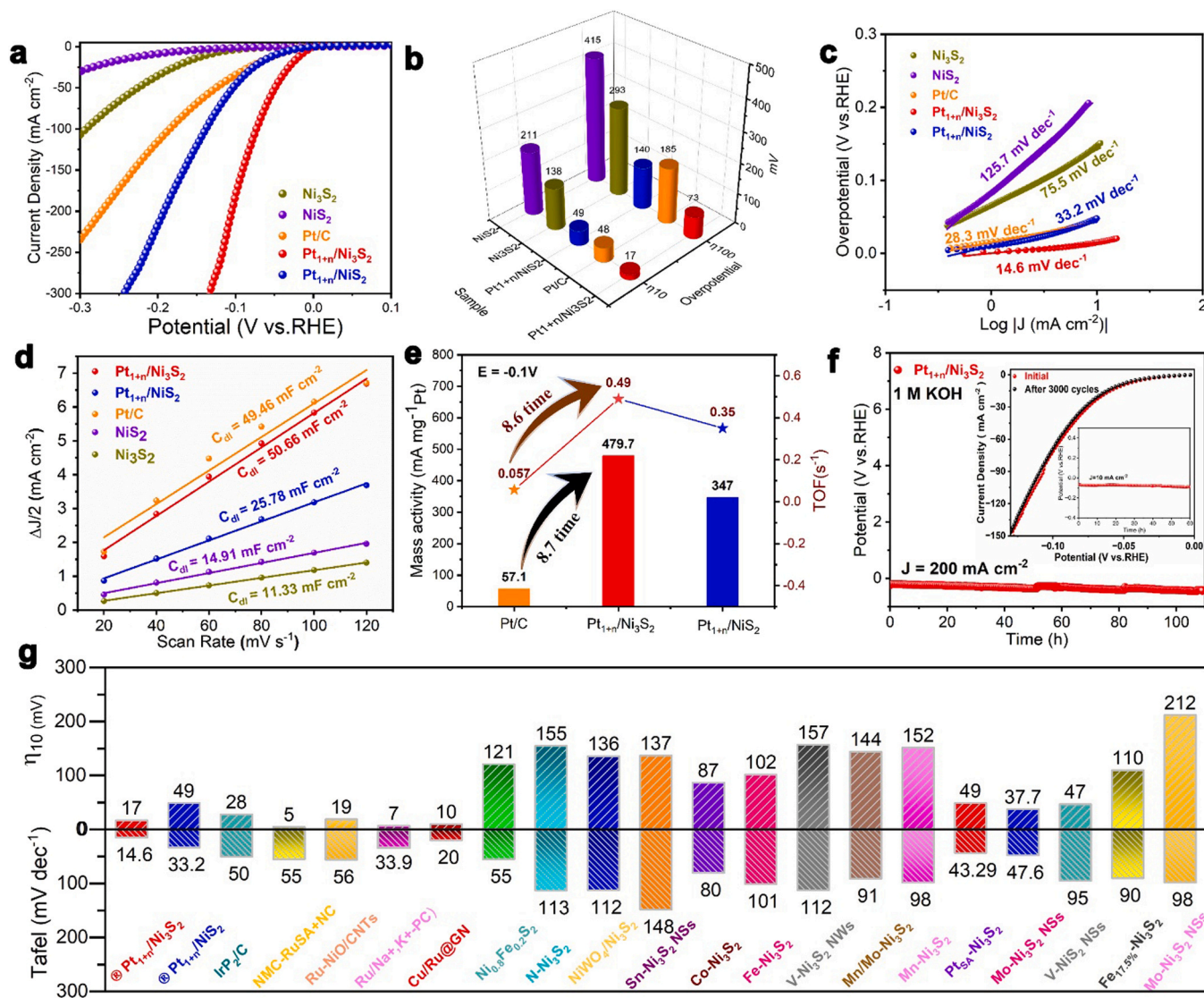**Fig. 4.** (a) The LSV curves of HER for Pt_{1+n}/Ni_3S_2, Pt_{1+n}/NiS_2, Pt/C, Ni_3S_2, and NiS_2 in 1 M KOH alkaline solution, respectively. (b) The overpotential comparisons for HER active at 10 and 100 mA cm^{-2}. (c) Tafel plot. (d) C_{dl} line-fitting curves. (e) The histogram images of mass activity (left) and TOF active (right) at overpotential of 100 mV. (f) The stability test curve of Pt_{1+n}/Ni_3S_2 electrocatalyst corresponding to 110 h at 200 mA cm^{-2} current density. The illustration showed the LSV curve before and after 3000 cycles CV measures and the stability test about 60 h at 10 mA cm^{-2} current density. (g) The parallel of the overpotential and Tafel value performance of excellent HER electrocatalyst reported at 10 mA cm^{-2} current density in 1 M KOH.

stable ADCs conditions. Meanwhile, the Pt, Ni, O and S element are uniform distributed on nanosheet after stability test for Pt_{1+n}/Ni_3S_2 (Fig. 5f). The results show that the morphology and crystal phase of Pt_{1+n}/Ni_3S_2 are extremely stable. Similarly, the $Ni(OH)_2$ (0 0 2) could be detected in both HRTEM and SAED, and the corresponding element about Pt, Ni and S are uniformly distributed on the nanosheet (Fig. S22). In addition, XPS analysis was applied to detect the oxidation states of Pt_{1+n}/Ni_3S_2 and Pt_{1+n}/NiS_2 corresponding elements after stability tests (Fig. S23a). As showed as Fig. 5g, it can be clearly found that Pt_{1+n}/Ni_3S_2 still detects Pt oxidation fitting peak at 72.3 eV, while Pt_{1+n}/NiS_2 has the slight tendency of left shift. For the Ni 2p orbits (Fig. 5h), the fitting peak nearby 854.8 eV is still attributed to Ni^{2+}, confirming the stability of Pt_{1+n}/Ni_3S_2. The M-S bonds are not change significantly for Pt_{1+n}/Ni_3S_2, while Pt_{1+n}/NiS_2 has negative shift of 0.6 eV due to large amount of dissolution of S (Table S6), which may be the reason for the difference in performance after the stability test (the inset in Fig. S18d). Finally, the fitting peaks are no significant shift in the O 1s spectrum (Fig. S23b). Therefore, the synthetic Pt_{1+n}/Ni_3S_2 ADCs have showed excellent structural stability and catalytic properties.

3.5. Kinetics research of Pt ADCs for alkaline HER

In-situ Raman spectroscopy is widely used to study the dynamic changes of surface substances and chemical bonds during reaction. As shown in Fig. 6a, weak δ_{Pt-OH} peaks are detected on the surface of Pt_{1+n}/Ni_3S_2 ADCs at 1062 cm^{-1} and no obvious change. The result shows that Pt-O bonds are derived from the Pt-OH axial ligand for Pt_{1+n}/Ni_3S_2 ADCs. Obviously, the H-O-H bending vibration peak at 1630 cm^{-1} shows that Pt_{1+n}/Ni_3S_2 ADCs are conducive to Volmer step and subsequent *OH desorption (Fig. 6b), resulting in good HER kinetic characteristics [28]. However, the peak intensity of Pt_{1+n}/NiS_2 ADCs at 1062 and 1630 cm^{-1} decreases with the decrease of voltage (Fig. S24), which confirms that Pt_{1+n}/NiS_2 ADCs only derived from *OH adsorption during HER reaction, and the desorption of Pt-*OH is blocked. It is consistent with the above results between the differences and coordination structure for Pt_{1+n}/Ni_3S_2 and Pt_{1+n}/NiS_2 ADCs. The larger stark tuning rate values indicate that the electrode has stronger adsorption effect on the adsorbent [57,58]. Therefore, to further clarify the effect of interfacial water on the performance of Pt ADCs, Gaussian fitting was
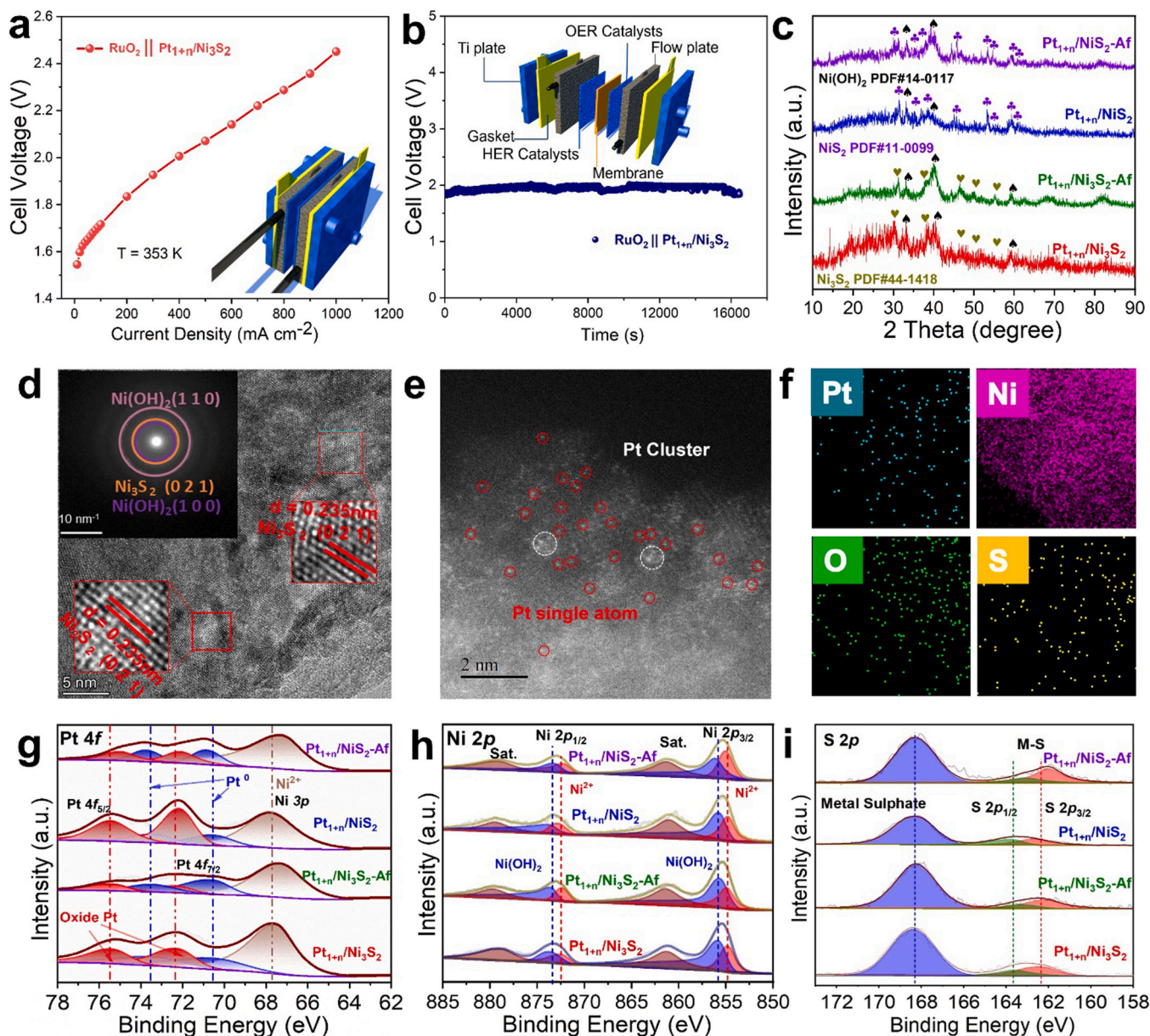
Fig. 5. (a) LSV curve measured in the AWE. The inset is a photograph of the AWE. (b) Durability test of $RuO_2 \parallel Pt_{1+n}/Ni_3S_2$ system in AWE device under 100 mA cm^{-2}. The inset is schematic diagram of AWE device. (c) The XRD of Pt_{1+n}/Ni_3S_2 and Pt_{1+n}/NiS_2, Pt_{1+n}/Ni_3S_2-Af and Pt_{1+n}/NiS_2-Af, respectively. "-Af " represented the corresponding sample after stability test. (d) The HRTEM pattern of Pt_{1+n}/Ni_3S_2 after stability test. The insert showed the SAED pattern. (e) The AC-STEM pattern of Pt_{1+n}/Ni_3S_2 after stability tests. Pt single atoms (red) and Pt clusters (white). (f) The element mapping pattern of Pt_{1+n}/Ni_3S_2 After stability tests. The XPS fine spectrum pictures about different catalysts after stability tests of (g) Pt 4 *f*, (h) Ni 2*p*, and (i) S 2*p* orbits, respectively.

performed on the O-H stretching mode (ν(O-H)) of interfacial water, and 4-HB-*H_2O, 2-HB-*H_2O and Pt-*H_2O stretching models were constructed (Fig. 6c and 6d, and Fig. S25a). As shown in Fig. 6e and Fig. S25b, Pt_{1+n}/Ni_3S_2 has stark tuning rate of about 48.3 cm^{-1}/V, indicating that the strong force on *H_2O is much higher than that on Pt_{1+n}/NiS_2. It is consistent with the results of the Raman adsorbed water strength on the Pt surface (Fig. S25c). In addition, attenuated total reflection-surface enhanced infrared absorption spectroscopy (ATR-SEIRAS) was used to further confirm the difference of reaction mechanism about Pt_{1+n}/Ni_3S_2 and Pt_{1+n}/NiS_2. As shown in Fig. 6f, the peaks of Pt_{1+n}/Ni_3S_2 ADCs between 1600 cm^{-1} and 3000–3600 cm^{-1} show significant red shift, indicating that the Pt-O_1Ni_1 active sites could generate strong adsorption effect on *H_2O and break the O-H bond more easily to accelerate the Volmer process [59,60]. However, Pt_{1+n}/NiS_2 does not show significant red shift, indicating that the Volmer process is not

promoted, which is consistent with the results of in-situ Raman analysis. Therefore, Pt_{1+n}/Ni_3S_2 ADCs with Pt-O_1Ni_1 atoms coordination have stronger water adsorption and desorption ability, and thus exhibit excellent alkaline HER activity.

3.6. Theoretical calculations

Density functional theory (DFT) calculations were used to reveal the difference in activity of Pt single atoms in different coordination environments of Pt_{1+n}/Ni_3S_2 and Pt_{1+n}/NiS_2. Therefore, the Ni_3S_2 (1 0 4) and NiS_2 (2 2 0) crystal faces were selected to construct atomic models of Pt_{1+n}/Ni_3S_2 with Pt-O_1Ni_1 coordination and Pt_{1+n}/NiS_2 with Pt-S_2Ni_2 coordination according to XRD, EXAFS and in-situ Raman results, respectively (Fig. 7a and b). It is well known that Pt sites exhibit poor HER performance in typical alkaline environments due to the limited
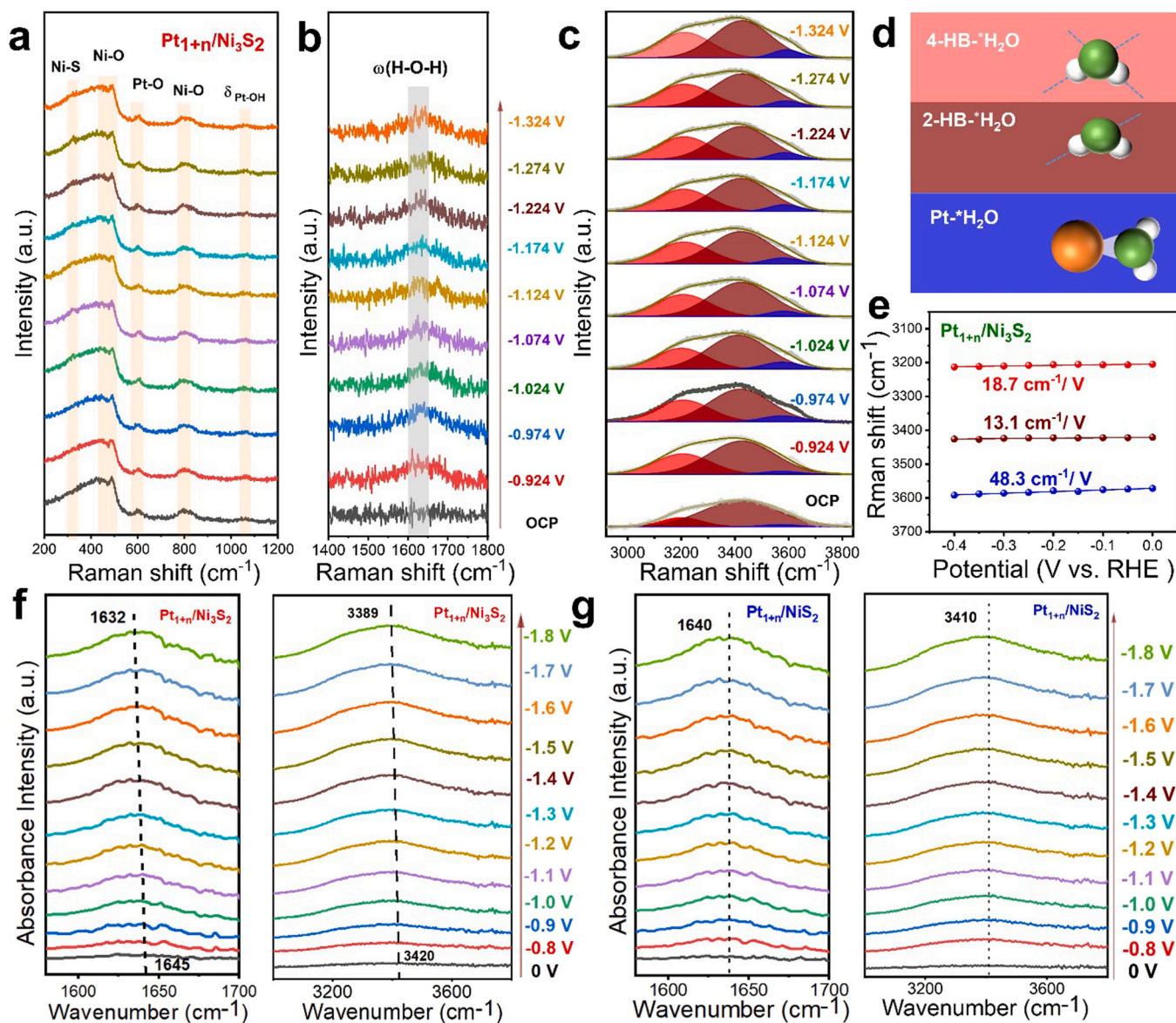
Fig. 6. (a, b) The in-situ Raman spectroscopy of Pt_{1+n}/Ni_3S_2 under different voltage. (c, d) In-situ Raman spectra of interface adsorbed water at Pt surfaces of Pt_{1+n}/Ni_3S_2. Gaussian fits of three different O–H stretching modes (ν_{O-H}) of symmetrical stretching vibration of water (4-HB-*H_2O), asymmetric stretching vibration of water (2-HB-*H_2O), and Pt-interface adsorbed water (Pt-*H_2O), were shown in light-red, vermilion, and light-blue, respectively. (e) Frequency plot of changes in the ν_{O-H} in Raman spectra of interfacial water at Pt surfaces of Pt_{1+n}/Ni_3S_2. In situ ATR-SEIRAS of (f) Pt_{1+n}/Ni_3S_2 and (g) Pt_{1+n}/NiS_2, respectively.

dissociation of water molecules [20]. As shown in Fig. 7c, Pt_{1+n}/Ni_3S_2 and Pt_{1+n}/NiS_2 exhibit the largest energy barrier difference during hydrolysis dissociation and Volmer mechanism is used as the rate-determining step. For Pt_{1+n}/Ni_3S_2, Pt sites could need to overcome the energy barrier of 0.11 eV combined with a proton H*, which is much lower than the 0.31 eV of Pt_{1+n}/NiS_2. It should be attributed to the fact that the O atoms with high electronegativity could as a proton H* acceptor and is rapidly delivered to the Pt site via Pt-O, which could accelerate the production of Pt-H* intermediate. It should be direct evidence that Pt_{1+n}/Ni_3S_2 and Pt_{1+n}/NiS_2 exhibit different alkaline HER properties, which is consistent with the previous analysis. In addition, the metal support interaction could be quantified by performing Bader charge analysis on the Pt and Ni atoms, confirming the electron transfer from Ni to Pt (Fig. 7d). Meanwhile, the charge transfers between Pt atom and Ni_3S_2 carrier is only 0.018 eV, which is lower than the 0.024 eV of Pt_{1+n}/NiS_2, indicating that is beneficial to weaken the binding of Ni_3S_2 carrier on Pt-H* to promote HER process by rapid transformation [50, 61]. The result indicates that the coordination, Pt single atom with the

high electronegative atom around clusters about Pt_{1+n}/Ni_3S_2, greatly improves the dissociation process of water molecule, exhibiting Volmer mechanism with better kinetics in alkaline environment than Pt_{1+n}/NiS_2 (Fig. 7e). Therefore, the coordination structure reported with the highly electronegative coordination for Pt single atoms provides a full prospect and vision for the design and development of high efficiency electrocatalysts for ADCs systems.

4. Conclusion

In summary, the work has constructed Pt ADCs with different coordination environment by varied vulcanization-electrodeposition strategy. Compared with Pt_{1+n}/NiS_2 with $Pt-S_2Ni_2$ single atom coordination environment, the Pt_{1+n}/Ni_3S_2 with $Pt-O_1Ni_1$ coordination structure requires lower overpotential of 17 and 73 mV to drive the current density of 10 and 100 mA cm^{-2}, respectively. Meanwhile, Pt_{1+n}/Ni_3S_2 displays the mass activity of 479.7 mA mg_{Pt}^{-1} and TOF of 0.49 $H_2\ s^{-1}$ under the overpotential of 100 mV, which are 8.7 and 8.6 times higher than that of
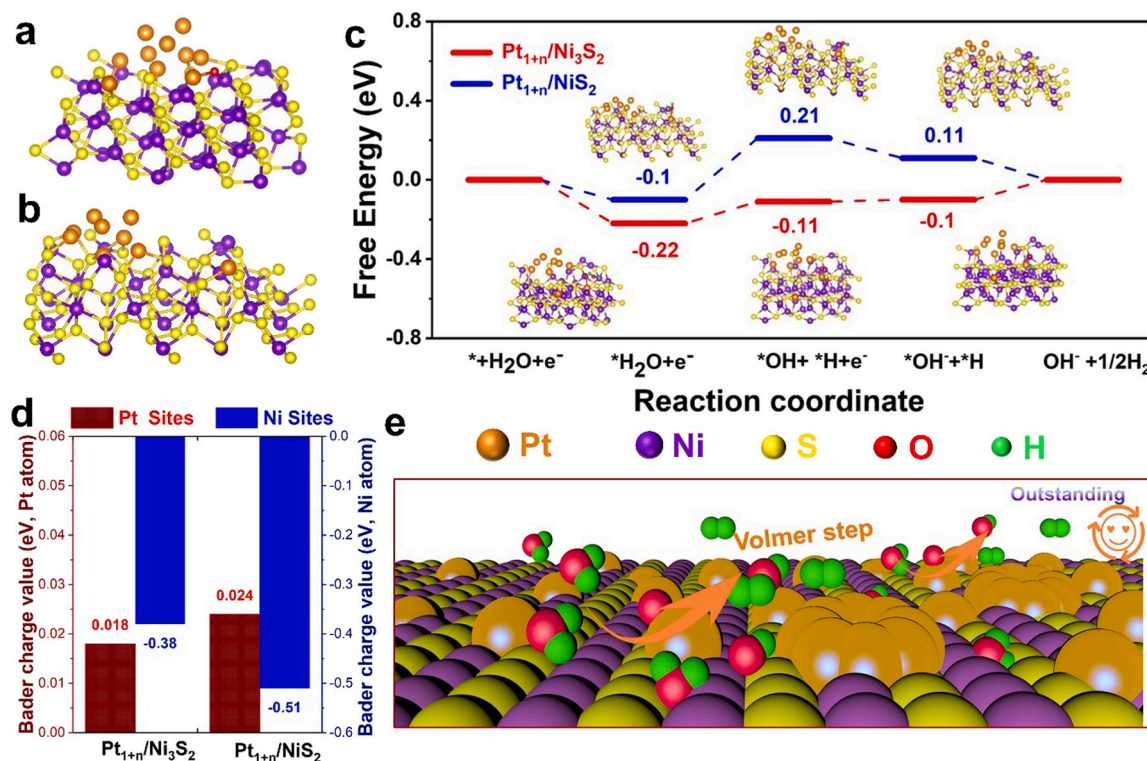
Fig. 7. The atomic structures of (a) Pt_{1+n}/Ni_3S_2 and (b) Pt_{1+n}/NiS_2, respectively. According to the results of HRTEM experiments, atomic models of Pt_{1+n}/Ni_3S_2 and Pt_{1+n}/NiS_2 were constructed by selecting Ni_3S_2 (1 0 4) and NiS_2 (2 2 0) crystal faces, respectively. (c) Free energy diagrams of HER on Pt_{1+n}/Ni_3S_2 and Pt_{1+n}/NiS_2, respectively. (d) The Bader charge of Pt_{1+n}/Ni_3S_2 and Pt_{1+n}/NiS_2 in Pt and Ni sites, respectively. (e) The schematic diagram of a possible HER mechanism for Pt_{1+n}/Ni_3S_2 with $Pt-O_1Ni_1$ structure. The orange, purple, yellow, red and green balls are for Pt, Ni, S, O and H atoms, respectively.

Pt/C, respectively. Besides, the assembled $RuO_2 \parallel Pt_{1+n}/Ni_3S_2$ system displays excellent water splitting performance in alkaline water electrolyzer. DFT studies and in-situ characterizations reveal that Pt_{1+n}/Ni_3S_2 ADCs with $Pt-O_1Ni_1$ single atoms has excellent HER activity because $Pt-O_1Ni_1$ are more likely to accelerate the production of Pt-H* at the Pt sites. Moreover, the high-density nanosheets also facilitate the full exposure and anchoring of Pt active sites, accelerating the mass transfer during HER process. This work provides a prospect and vision for the structure-activity relationship between atomic coordination and alkaline HER activity in atomically dispersed catalysts systems and promotes the development of highly active electrocatalysts in alkaline water splitting.

CRediT authorship contribution statement

Dengfeng Wu: Resources, Software, Writing – review & editing, Funding acquisition. **Liang Qiao:** Funding acquisition, Resources, Validation, Visualization. **Wei Xia:** Investigation, Methodology, Software, Validation, Writing – original draft. **Kebin Chi:** Investigation, Methodology, Project administration, Validation, Visualization. **Mengyao Ma:** Data curation, Investigation, Visualization. **Xiaoyan Guo:** Investigation, Methodology, Validation, Visualization. **Tianpeng Liu:** Data curation, Methodology, Resources, Software, Validation, Visualization. **Zhenhao Li:** Funding acquisition, Investigation, Resources, Validation. **Dong Cao:** Conceptualization, Data curation, Funding acquisition, Resources, Writing – original draft, Writing – review & editing. **Daojian Cheng:** Project administration, Resources, Supervision, Writing – review & editing.

Declaration of Competing Interest

The authors declare no conflict of interest.

Data Availability

Data will be made available on request.

Appendix A. Supporting information

Supplementary data associated with this article can be found in the online version at doi:10.1016/j.apcatb.2024.124074.

References

[1] X. Tian, P. Zhao, W. Sheng, Hydrogen evolution and oxidation: mechanistic studies and material advances, Adv. Mater. 31 (2019) e1808066, https://doi.org/10.1002/adma.201808066.

[2] H.Q. Fu, M. Zhou, P.F. Liu, P. Liu, H. Yin, K.Z. Sun, H.G. Yang, M. Al-Mamun, P. Hu, H.F. Wang, H. Zhao, Hydrogen spillover-bridged volmer/tafel processes enabling ampere-level current density alkaline hydrogen evolution reaction under low overpotential, J. Am. Chem. Soc. 144 (2022) 6028–6039, https://doi.org/10.1021/jacs.2c01094.

[3] T. Cui, J. Chi, J. Zhu, X. Sun, J. Lai, Z. Li, L. Wang, Tuning the size and chemisorption of FeP4 by trace Ru doping for hydrazine-assisted hydrogen evolution in seawater at large-current-density, Appl. Catal. B Environ. 319 (2022) 121950, https://doi.org/10.1016/j.apcatb.2022.121950.

[4] X. Du, J. Huang, J. Zhang, Y. Yan, C. Wu, Y. Hu, C. Yan, T. Lei, W. Chen, C. Fan, J. Xiong, Modulating electronic structures of inorganic nanomaterials for efficient electrocatalytic water splitting, Angew. Chem. Int. Ed. 58 (2019) 4484–4502, https://doi.org/10.1002/anie.201810104.

[5] F. Zhang, Y. Zhu, Q. Lin, L. Zhang, X. Zhang, H. Wang, Noble-metal single-atoms in thermocatalysis, electrocatalysis, and photocatalysis, Energy Environ. Sci. 14 (2021) 2954–3009, https://doi.org/10.1039/d1ee00247c.

[6] S. Huang, Y. Meng, Y. Cao, F. Yao, Z. He, X. Wang, H. Pan, M. Wu, Amorphous NiWO$_4$ nanoparticles boosting the alkaline hydrogen evolution performance of Ni$_3$S$_2$ electrocatalysts, Appl. Catal. B Environ. 274 (2020) 119120, https://doi.org/10.1016/j.apcatb.2020.119120.

[7] Z. Pu, J. Zhao, I.S. Amiinu, W. Li, M. Wang, D. He, S. Mu, A universal synthesis strategy for P-rich noble metal diphosphide-based electrocatalysts for the hydrogen evolution reaction, Energy Environ. Sci. 12 (2019) 952–957, https://doi.org/10.1039/c9ee00197b.

[8] S. Bai, M. Xie, T. Cheng, K. Cao, Y. Xu, X. Huang, Surface engineering of RhOOH nanosheets promotes hydrogen evolution in alkaline, Nano Energy 78 (2020) 105224, https://doi.org/10.1016/j.nanoen.2020.105224.

[9] A.M. Harzandi, S. Shadman, M. Ha, C.W. Myung, D.Y. Kim, H.J. Park, S. Sultan, W.-S. Noh, W. Lee, P. Thangavel, W.J. Byun, S.-h Lee, J.N. Tiwari, T.J. Shin, J.-H. Park, Z. Lee, J.S. Lee, K.S. Kim, Immiscible bi-metal single-atoms driven synthesis of electrocatalysts having superb mass-activity and durability, Appl. Catal. B Environ. 270 (2020) 118896, https://doi.org/10.1016/j.apcatb.2020.118896.

[10] H. Jin, M. Ha, M.G. Kim, J.H. Lee, K.S. Kim, Engineering Pt coordination environment with atomically dispersed transition metal sites toward superior hydrogen evolution, Adv. Energy Mater. 13 (2023) 202204213, https://doi.org/10.1002/aenm.202204213.

[11] M. Duan, T. Shu, Z. Li, D. Zhang, L.-Y. Gan, K.X. Yao, Q. Yuan, Boosting alkaline hydrogen evolution performance by constructing ultrasmall Ru clusters/Na$^+$, K$^+$-decorated porous carbon composites, Nano Res 16 (2023) 8836–8844, https://doi.org/10.1007/s12274-023-5558-5.

[12] J. Wang, T. Liao, Z. Wei, J. Sun, J. Guo, Z. Sun, Heteroatom-doping of non-noble metal-based catalysts for electrocatalytic hydrogen evolution: an electronic structure tuning strategy, Small Methods 5 (2021) e2000988, https://doi.org/10.1002/smtd.202000988.

[13] G.H. Gu, J. Lim, C. Wan, T. Cheng, H. Pu, S. Kim, J. Noh, C. Choi, J. Kim, W. A. Goddard 3rd, X. Duan, Y. Jung, Autobifunctional mechanism of jagged Pt nanowires for hydrogen evolution kinetics via end-to-end simulation, J. Am. Chem. Soc. 143 (2021) 5355–5363, https://doi.org/10.1021/jacs.0c11261.

[14] S. Zhu, X. Qin, F. Xiao, S. Yang, Y. Xu, Z. Tan, J. Li, J. Yan, Q. Chen, M. Chen, M. Shao, The role of ruthenium in improving the kinetics of hydrogen oxidation and evolution reactions of platinum, Nat. Catal. 4 (2021) 711–718, https://doi.org/10.1038/s41929-021-00663-5.

[15] Dan Li, Xufang Chen, Yaozha Lv, Guoyang Zhang, Yu Huang, Wei Liu, Yang Li, Rongsheng Chen, Colin Nuckolls, Hongwei Ni, An effective hybrid electrocatalyst for the alkaline HER: Highly dispersed Pt sites immobilized by a functionalized NiRu-hydroxide, Appl. Catal. B Environ. 269 (2020) 118824, https://doi.org/10.1016/j.apcatb.2020.118824.

[16] S. Chen, S. Wang, P. Hao, M. Li, Y. Zhang, J. Guo, W. Ding, M. Liu, J. Wang, X. Guo, N,O-C Nanocage-mediated high-efficient hydrogen evolution reaction on IrNi@N, O-C electrocatalyst, Appl. Catal. B Environ. 304 (2022) 120996, https://doi.org/10.1016/j.apcatb.2021.120996.

[17] N.K. Dang, M. Umer, P. Thangavel, S. Sultan, J.N. Tiwari, J.H. Lee, M.G. Kim, K. S. Kim, Surface enrichment of iridium on IrCo alloys for boosting hydrogen production, J. Mater. Chem. A 9 (2021) 16898–16905, https://doi.org/10.1039/d1ta02597j.

[18] N. Yao, R. Meng, F. Wu, Z. Fan, G. Cheng, W. Luo, Oxygen-vacancy-induced CeO$_2$/Co$_4$N heterostructures toward enhanced pH-Universal hydrogen evolution reactions, Appl. Catal. B Environ. 277 (2020) 119282, https://doi.org/10.1016/j.apcatb.2020.119282.

[19] P. Zhou, G. Hai, G. Zhao, R. Li, X. Huang, Y. Lu, G. Wang, CeO$_2$ as an "electron pump" to boost the performance of Co$_4$N in electrocatalytic hydrogen evolution, oxygen evolution and biomass oxidation valorization, Appl. Catal. B Environ. 325 (2023) 119282, https://doi.org/10.1016/j.apcatb.2023.122364.

[20] A. Pei, R. Xie, Y. Zhang, Y. Feng, W. Wang, S. Zhang, Z. Huang, L. Zhu, G. Chai, Z. Yang, Q. Gao, H. Ye, C. Shang, B.H. Chen, Z. Guo, Effective electronic tuning of Pt single atoms via heterogeneous atomic coordination of (Co,Ni)(OH)$_2$ for efficient hydrogen evolution, Energy Environ. Sci. 16 (2023) 1035–1048, https://doi.org/10.1039/d2ee02785b.

[21] S. Park, Y.-L. Lee, Y. Yoon, S.Y. Park, S. Yim, W. Song, S. Myung, K.-S. Lee, H. Chang, S.S. Lee, K.-S. An, Reducing the high hydrogen binding strength of vanadium carbide MXene with atomic Pt confinement for high activity toward HER, Appl. Catal. B Environ. 304 (2022) 120989, https://doi.org/10.1016/j.apcatb.2021.120989.

[22] Z. Yu, Y. Li, A. Torres-Pinto, A.P. LaGrow, V.M. Diaconescu, L. Simonelli, M. J. Sampaio, O. Bondarchuk, I. Amorim, A. Araujo, A.M.T. Silva, C.G. Silva, J. L. Faria, L. Liu, Single-atom Ir and Ru anchored on graphitic carbon nitride for efficient and stable electrocatalytic/photocatalytic hydrogen evolution, Appl. Catal. B Environ. 310 (2022) 121318, https://doi.org/10.1016/j.apcatb.2022.121318.

[23] L. Sun, V. Reddu, X. Wang, Multi-atom cluster catalysts for efficient electrocatalysis, Chem. Soc. Rev. 51 (2022) 8923–8956, https://doi.org/10.1039/d2cs00233g.

[24] C. Yang, Z. Wu, Z. Zhao, Y. Gao, T. Ma, C. He, C. Wu, X. Liu, X. Luo, S. Li, C. Cheng, C. Zhao, Electronic structure-dependent water-dissociation pathways of ruthenium-based catalysts in alkaline H$_2$ evolution, Small 19 (2023) e2206949, https://doi.org/10.1002/smll.202206949.

[25] Y. Zhao, P.V. Kumar, X. Tan, X. Lu, X. Zhu, J. Jiang, J. Pan, S. Xi, H.Y. Yang, Z. Ma, T. Wan, D. Chu, W. Jiang, S.C. Smith, R. Amal, Z. Han, X. Lu, Modulating Pt-O-Pt atomic clusters with isolated cobalt atoms for enhanced hydrogen evolution

[26] Y. Guo, M. Wang, Q. Zhu, D. Xiao, D. Ma, Ensemble effect for single-atom, small cluster and nanoparticle catalysts, Nat. Catal. 5 (2022) 766–776, https://doi.org/10.1038/s41929-022-00839-7.

[27] Y. Gao, D. Wang, Atomically Dispersed Catalysts: Precise Synthesis, Structural Regulation, and Structure–Activity Relationship, CCS Chem. (2023) 1–23, https://doi.org/10.31635/ccschem.023.202303236.

[28] T. Zhang, J. Jin, J. Chen, Y. Fang, X. Han, J. Chen, Y. Li, Y. Wang, J. Liu, L. Wang, Pinpointing the axial ligand effect on platinum single-atom-catalyst towards efficient alkaline hydrogen evolution reaction, Nat. Commun. 13 (2022) 6875, https://doi.org/10.1038/s41467-022-34619-5.

[29] A. Pei, G. Li, L. Zhu, Z. Huang, J. Ye, Y.C. Chang, S.M. Osman, C.W. Pao, Q. Gao, B. H. Chen, R. Luque, Nickel hydroxide-supported Ru single atoms and Pd nanoclusters for enhanced electrocatalytic hydrogen evolution and ethanol oxidation, Adv. Funct. Mater. 32 (2022) 2208587, https://doi.org/10.1002/adfm.202208587.

[30] J. Wu, W. Zhong, C. Yang, W. Xu, R. Zhao, H. Xiang, Q. Zhang, X. Li, N. Yang, Sulfur-vacancy rich nonstoichiometric TiS$_{2−x}$/NiS heterostructures for superior universal hydrogen evolution, Appl. Catal. B Environ. 310 (2022) 121332, https://doi.org/10.1016/j.apcatb.2022.121332.

[31] H. Yao, X. Wang, K. Li, C. Li, C. Zhang, J. Zhou, Z. Cao, H. Wang, M. Gu, M. Huang, H. Jiang, Strong electronic coupling between ruthenium single atoms and ultrafine nanoclusters enables economical and effective hydrogen production, Appl. Catal. B Environ. 312 (2022) 121378, https://doi.org/10.1016/j.apcatb.2022.121378.

[32] H. Jin, S. Sultan, M. Ha, J.N. Tiwari, M.G. Kim, K.S. Kim, Simple and scalable mechanochemical synthesis of noble metal catalysts with single atoms toward highly efficient hydrogen evolution, Adv. Funct. Mater. 30 (2020) 2000531, https://doi.org/10.1002/adfm.202000531.

[33] J.N. Tiwari, A.M. Harzandi, M. Ha, S. Sultan, C.W. Myung, H.J. Park, D.Y. Kim, P. Thangavel, A.N. Singh, P. Sharma, S.S. Chandrasekaran, F. Salehnia, J.W. Jang, H.S. Shin, Z. Lee, K.S. Kim, High-performance hydrogen evolution by Ru single atoms and nitrided-ru nanoparticles implanted on N-doped graphitic sheet, Adv. Energy Mater. 9 (2019) 201900931, https://doi.org/10.1002/aenm.201900931.

[34] J. Zhao, Y. Zhang, Y. Xia, B. Zhang, Y. Du, B. Song, H.-L. Wang, S. Li, P. Xu, Strong phosphide-metaphosphate interaction in RuP/CoNiP$_4$O$_{12}$ for enhanced electrocatalytic water splitting, Appl. Catal. B Environ. 328 (2023) 122447, https://doi.org/10.1016/j.apcatb.2023.122447.

[35] W. He, X. Zhang, K. Zheng, C. Wu, Y. Pan, H. Li, L. Xu, R. Xu, W. Chen, Y. Liu, C. Wang, Z. Sun, S. Wei, Structural evolution of anatase-supported platinum nanoclusters into a platinum-titanium intermetallic containing platinum single atoms for enhanced catalytic CO oxidation, Angew. Chem. Int. Ed. 62 (2023) e202213365, https://doi.org/10.1002/anie.202213365.

[36] D. Cao, Z. Zhang, Y. Cui, R. Zhang, L. Zhang, J. Zeng, D. Cheng, One-step approach for constructing high-density single-atom catalysts toward overall water splitting at industrial current densities, Angew. Chem. Int. Ed. 62 (2023) e202214259, https://doi.org/10.1002/anie.202214259.

[37] K.L. Zhou, Z. Wang, C.B. Han, X. Ke, C. Wang, Y. Jin, Q. Zhang, J. Liu, H. Wang, H. Yan, Platinum single-atom catalyst coupled with transition metal/metal oxide heterostructure for accelerating alkaline hydrogen evolution reaction, Nat. Commun. 12 (2021) 3783, https://doi.org/10.1038/s41467-021-24079-8.

[38] H. Irshad;, J. Munichandraiah, Electrodeposited nickel–cobalt–sulfide catalyst for the hydrogen evolution reaction, ACS Appl. Mater. Interfaces 9 (2017) 19746–19755, https://doi.org/10.1038/s41586-021-03870-z.

[39] Y. Qin, H. Zhuo, X. Liang, K. Yu, Y. Wang, D. Gao, X. Zhang, Surface-modified Pt$_1$Ni$_1$–Ni(OH)$_2$ nanoparticles with abundant Pt–Ni(OH)$_2$ interfaces enhance electrocatalytic properties, Dalton Trans. 48 (2019) 10313–10319, https://doi.org/10.1039/c9dt01536a.

[40] C. Wan, Z. Zhang, J. Dong, M. Xu, H. Pu, D. Baumann, Z. Lin, S. Wang, J. Huang, A. H. Shah, X. Pan, T. Hu, A.N. Alexandrova, Y. Huang, X. Duan, Amorphous nickel hydroxide shell tailors local chemical environment on platinum surface for alkaline hydrogen evolution reaction, Nat. Mater. 22 (2023) 1022–1029, https://doi.org/10.1038/s41563-023-01584-3.

[41] B. Ruqia, S.I. Choi, Pt and Pt–Ni(OH)$_2$ electrodes for the hydrogen evolution reaction in alkaline electrolytes and their nanoscaled electrocatalysts, ChemSusChem 11 (2018) 2643–2653, https://doi.org/10.1002/cssc.201800781.

[42] Y. Bian, Y. Wang, Z. Gao, J. Hu, D. Liu, L. Dai, A facile approach to high-performance trifunctional electrocatalysts by substrate-enhanced electroless deposition of Pt/NiO/Ni on carbon nanotubes, Nanoscale 12 (2020) 14615–14625, https://doi.org/10.1039/d0nr03378b.

[43] Z. Zhao, H. Liu, W. Gao, W. Xue, Z. Liu, J. Huang, X. Pan, Y. Huang, Surface-engineered PtNi-O nanostructure with record-high performance for electrocatalytic hydrogen evolution reaction, J. Am. Chem. Soc. 140 (2018) 9046–9050, https://doi.org/10.1021/jacs.8b04770.

[44] S. Sun, Y.-C. Zhang, G. Shen, Y. Wang, X. Liu, Z. Duan, L. Pan, X. Zhang, J.-J. Zou, Photoinduced composite of Pt decorated Ni(OH)$_2$ as strongly synergetic cocatalyst to boost H$_2$O activation for photocatalytic overall water splitting, Appl. Catal. B Environ. 243 (2019) 253–261, https://doi.org/10.1016/j.apcatb.2018.10.051.

[45] D. Cao, D. Xu, D. Cheng, Branch-leaf-shaped CuNi@NiFeCu nanodendrites as highly efficient electrocatalysts for overall water splitting, Appl. Catal. B Environ. 298 (2021) 120600, https://doi.org/10.1016/j.apcatb.2021.120600.

[46] J. Liu, J. Wang, B. Zhang, Y. Ruan, L. Lv, X. Ji, K. Xu, L. Miao, J. Jiang, Hierarchical NiCo$_2$S$_4$@NiFe LDH Heterostructures Supported on Nickel Foam for Enhanced Overall-Water-Splitting Activity, ACS Appl. Mater. Interfaces 9 (2017) 15364–15372, https://doi.org/10.1021/acsami.7b00019.

[47] T. Liu, W. Liu, M. Ma, L. Guo, R. Cui, D. Cheng, D. Cao, Constructing nickel vanadium phosphide nanoarrays with highly active heterointerfaces for water oxidation in alkali media, Electrochim. Acta 439 (2023) 141721, https://doi.org/10.1016/j.electacta.2022.141721.

[48] X. Li, Z. Kou, S. Xi, W. Zang, T. Yang, L. Zhang, J. Wang, Porous NiCo$_2$S$_4$/FeOOH nanowire arrays with rich sulfide/hydroxide interfaces enable high OER activity, Nano Energy 78 (2020) 105230, https://doi.org/10.1016/j.nanoen.2020.105230.

[49] W. Zhu, W. Chen, H. Yu, Y. Zeng, F. Ming, H. Liang, Z. Wang, NiCo/NiCo–OH and NiFe/NiFe–OH core shell nanostructures for water splitting electrocatalysis at large currents, Appl. Catal. B Environ. 278 (2020) 119326, https://doi.org/10.1016/j.apcatb.2020.119326.

[50] K.L. Zhou, C.B. Han, Z. Wang, X. Ke, C. Wang, Y. Jin, Q. Zhang, J. Liu, H. Wang, H. Yan, Atomically dispersed platinum modulated by sulfide as an efficient electrocatalyst for hydrogen evolution reaction, Adv. Sci. 8 (2021) 2100347, https://doi.org/10.1002/advs.202100347.

[51] W.W. Lonergan, D.G. Vlachos, J.G. Chen, Correlating extent of Pt–Ni bond formation with low-temperature hydrogenation of benzene and 1,3-butadiene over supported Pt/Ni bimetallic catalysts, J. Catal. 271 (2010) 239–250, https://doi.org/10.1016/j.jcat.2010.01.019.

[52] T. He, W. Wang, F. Shi, X. Yang, X. Li, J. Wu, Y. Yin, M. Jin, Mastering the surface strain of platinum catalysts for efficient electrocatalysis, Nature 598 (2021) 76–81, https://doi.org/10.1038/s41586-021-03870-z.

[53] Q. Li, D. Wang, C. Han, X. Ma, Q. Lu, Z. Xing, X. Yang, Construction of amorphous interface in an interwoven NiS/NiS$_2$ structure for enhanced overall water splitting, J. Mater. Chem. A 6 (2018) 8233–8237, https://doi.org/10.1039/c8ta01928b.

[54] S. Anantharaj, S. Noda, M. Driess, P.W. Menezes, The pitfalls of using potentiodynamic polarization curves for tafel analysis in electrocatalytic water splitting, ACS Energy Lett. 16 (2021) 1607–1611, https://doi.org/10.1021/acsenergylett.1c00608.

[55] Z. Xiao, Y. Wang, Y.-C. Huang, Z. Wei, C.-L. Dong, J. Ma, S. Shen, Y. Li, S. Wang, Filling the oxygen vacancies in Co$_3$O$_4$ with phosphorus: an ultra-efficient electrocatalyst for overall water splitting, Energy Environ. Sci. 10 (2017) 2563–2569, https://doi.org/10.1039/c7ee01917c.

[56] S. Anantharaj, S.R. Ede, K. Sakthikumar, K. Karthick, S. Mishra, S. Kundu, Recent trends and perspectives in electrochemical water splitting with an emphasis on sulfide, selenide, and phosphide catalysts of Fe, Co, and Ni: a review, ACS Catal. 6 (2016) 8069–8097, https://doi.org/10.1021/acscatal.6b02479.

[57] X. Chen, X.-T. Wang, J.-B. Le, S.-M. Li, X. Wang, Y.-J. Zhang, P. Radjenovic, Y. Zhao, Y.-H. Wang, X.-M. Lin, J.-C. Dong, J.-F. Li, Revealing the role of interfacial water and key intermediates at ruthenium surfaces in the alkaline hydrogen evolution reaction, Nat. Commun. 14 (2023) 5289, https://doi.org/10.1038/s41467-023-41030-1.

[58] Y.-H. Wang, S. Zheng, W.-M. Yang, R.-Y. Zhou, Q.-F. He, P. Radjenovic, J.-C. Dong, S. Li, J. Zheng, Z.-L. Yang, G. Attard, F. Pan, Z.-Q. Tian, J.-F. Li, In situ Raman spectroscopy reveals the structure and dissociation of interfacial water, Nature 600 (2021) 81–85, https://doi.org/10.1038/s41586-021-04068-z.

[59] J. Liu, Z. Wang, X. Wu, D. Zhang, Y. Zhang, J. Xiong, Z. Wu, J. Lai, L. Wang, Pt doping and strong metal–support interaction as a strategy for NiMo-based electrocatalysts to boost the hydrogen evolution reaction in alkaline solution, J. Mater. Chem. A 10 (2022) 15395–15401, https://doi.org/10.1039/d2ta03934f.

[60] X. Yang, M. Xi, X. Guo, X. Shen, Z. Liu, H. Jiang, Y. Zhu, Ni–CeO$_2$ heterostructure promotes hydrogen evolution reaction via tuning of the O−H bond length of adsorbed water at the electrolyte/electrode interface, ChemSusChem 16 (2023), https://doi.org/10.1002/cssc.202300348.

[61] S. Fang, X. Zhu, X. Liu, J. Gu, W. Liu, D. Wang, W. Zhang, Y. Lin, J. Lu, S. Wei, Y. Li, T. Yao, Uncovering near-free platinum single-atom dynamics during electrochemical hydrogen evolution reaction, Nat. Commun. 11 (2020) 1029, https://doi.org/10.1038/s41467-020-14848-2.